



# Reduced-basis boundary element method for fast electromagnetic field computation

YATING SHI, XIUGUO CHEN,\*  YINYIN TAN, HAO JIANG, AND SHIYUAN LIU

State Key Laboratory of Digital Manufacturing Equipment and Technology, Huazhong University of Science and Technology, Wuhan, Hubei 430074, China

\*Corresponding author: xiuguo.chen@hust.edu.cn

Received 25 May 2017; revised 12 October 2017; accepted 2 November 2017; posted 6 November 2017 (Doc. ID 296708); published 27 November 2017

**In this work, we combine conventional boundary element method (BEM) with the reduced-basis method (RBM) and propose a reduced-basis boundary element method (RB-BEM) to realize efficient modeling for parameterized electromagnetic scattering problems of dielectric scatterers. The RB-BEM allows for splitting the modeling process into a parameter-independent offline part and parameter-dependent online part, and replacing the high-dimensional original model obtained by conventional BEM with a low-dimensional reduced-basis model to improve computational efficiency of the online part. We also propose an improved greedy algorithm based on multi-grid to improve the computational efficiency of the offline part. The numerical experiments indicate that the efficiency of the improved greedy algorithm is several times higher than that of the standard one, and the solving efficiency of the reduced-basis model is several times to dozens of times higher than that of the original model with a prescribed approximation accuracy.** © 2017 Optical Society of America

**OCIS codes:** (290.5825) Scattering theory; (260.2110) Electromagnetic optics; (050.1755) Computational electromagnetic methods.

<https://doi.org/10.1364/JOSAA.34.002231>

## 1. INTRODUCTION

Fast and efficient modeling of electromagnetic fields is highly desirable in many cases, such as optimal design [1,2] and model-based optical metrology [3,4], where the distribution of electromagnetic fields is typically repeatedly calculated under a parameterized context. The parameters here could be the wavelength and incident angle of an illuminating wave, and/or the geometric parameters of a scatterer under study. Various computational electromagnetic methods have been developed over the past decades to calculate the scattered electromagnetic fields, including semi-analytical rigorous coupled-wave analysis [5–7], which is specially developed to model the electromagnetic fields scattered from a periodic scatterer, and numerical methods such as the finite element method (FEM), finite-difference time-domain (FDTD) method, and the boundary element method (BEM), also called the method of moment [7–15]. These numerical approaches could be roughly classified into a category based on solving partial differential equations (PDEs) such as FEM and FDTD, as well as a category based on solving integral equations such as BEM. Despite their widespread applications, these brute force numerical approaches are usually computationally too expensive to satisfy the practical efficiency requirement in the above-mentioned many-query or real-time context.

Many model order reduction techniques such as modal expansion [16], asymptotic waveform evaluation [17,18], Padé via Lanczos model reduction [19], and the Krylov subspace method [20] have been proposed for combination with the brute force approaches to reduce the complexity of the involved models. Another numerical technique, called the reduced-basis method (RBM), was originally introduced in [21,22] whereby the approximate space, which was used to reduce the dimension of the original model obtained by brute force methods, was local and typically low-dimensional in the number of parameters. Recently, the RBM has overcome limitations, showing great potential in rapidly solving parameterized PDEs with the introduction of the assumption of parameter affine decomposition [23–27] and gaining wide applications in mechanics, fluid dynamics, electromagnetic, etc. [28–32].

In RBM, a high-dimensional model obtained by directly applying the brute force numerical methods to the problem under study is first projected into a low-dimensional reduced-basis space; it then is replaced with a low-dimensional, reduced-basis model. In addition, by assuming that all the parameter-dependent operators satisfy an assumption of parameter affine decomposition, the RBM splits the modeling process into a parameter-independent offline part and parameter-dependent online part. In the online phase, one only need do a few

parameter-dependent linear calculations to construct and solve the reduced-basis model, which thereby dramatically improves the computational efficiency compared to the brute force numerical methods.

In this work, we combine conventional BEM with RBM and propose a reduced-basis boundary element method (RB-BEM) to realize efficient modeling of the electromagnetic fields scattered by dielectric scatterers. Currently, the majority of research on RBM in electromagnetic scattering problems mainly focuses on its combination with FEM [28–30]. Comparing with FEM, the BEM might be preferable to electromagnetic scattering problems because of its inherent advantages such as decreasing the dimension of a scattering problem by limiting its unknown variables only on the boundaries of the scatterer, and modeling scattering problems without pre-setting additional absorbing conditions. Although the literature has witnessed the combination of RBM with the boundary integral equations for the electromagnetic scattering of perfect electric conductors [31,32], to the best of our knowledge, it is difficult to deduce such integral forms for more general cases such as the dielectric scatterers. For these more general cases, the parameter-dependent operators do not naturally satisfy the parameter affine decomposition assumption. To this end, we apply an empirical interpolation method (EIM) [33,34] to construct interpolation expressions which satisfy the affine decomposition assumption to realize the offline–online decomposition in the modeling process.

In the framework of RBM, the greedy algorithm introduced in [24] is commonly used to construct the affine decomposition expressions of parameter-dependent forms and the reduced-basis space. As a grid-based iterative method, the efficiency of the greedy algorithm linearly depends on the size of the training set, which is sampled from the parameter domain. To improve the efficiency, especially in high-dimensional parameter spaces, various improved greedy algorithms are proposed. Benefitting from the development of computer hardware, Knezevic and Peterson [35] developed a parallel strategy to enhance the efficiency by sacrificing computational resource. Adaptive procedures [36] based on a coarse training set prevent execution of the greedy algorithm over the well-enough training set, and therefore significantly decrease the workload of the greedy algorithm. Hesthaven *et al.* [37] proposed a method which dynamically controlled the size of the training set at each step of the greedy algorithm based on a saturation assumption of the approximation error.

In this work, we propose an improved greedy algorithm which is based on multiple training sets with increased dimensions. The principle is to construct an approximate space with certain accuracy by running the greedy algorithm over the smallest training set, and then train the space over a larger training set to reach the required accuracy. Since most of the bases of the approximate space are selected from the coarse training set, the workload of the greedy algorithm is expected to be significantly decreased. To further improve the efficiency, we also combine our improved greedy algorithm with the method in [37] to decrease the workload at each step of the algorithm.

This paper is organized as follows. In Section 2, we briefly describe the two-dimensional (2D) and three-dimensional (3D)

electro-magnetic scattering problems solved by conventional BEM. For the sake of clarity, we assume that all the scatterers under study in this paper are homogeneous or piecewise homogeneous. In Section 3, we briefly describe the principle of RBM, and then the improved greedy algorithms are introduced to efficiently construct the low-dimensional reduced-basis space. In Section 4, we present the RB-BEM for both 2D and 3D dielectric scatterers. Four numerical examples are presented in Section 5 to verify the proposed RB-BEM. Some conclusions are finally drawn in Section 6.

## 2. BOUNDARY ELEMENT METHOD

### A. 2D Electromagnetic Scattering Problem

The 2D electromagnetic problem can be formulated as a scalar problem described by the scalar Helmholtz equation. Let us consider the problem of a scalar wave produced by a source in the presence of a dielectric scatterer immersed in a homogeneous medium, and the source and the scatterer are invariable along the  $z$  axis (the direction that is perpendicular to the paper surface). In this case, we only need to consider a plane perpendicular to the  $z$  axis, which can be decomposed into several piecewise homogeneous regions. Assume that the  $b$ -th homogeneous region  $\Omega_b$  is surrounded by boundaries  $\Gamma_{b1}, \dots, \Gamma_{bL}$ , and a source is placed in  $\Omega_b$ ; then the scalar wave field  $u$  satisfies the following boundary integral equation (BIE) [10,11]:

$$u^{\text{inc}}(\mathbf{r}) + \sum_{i=1}^L (\mathcal{S}_{bi}u)(\mathbf{r}) - (\mathcal{F}_{bi}u)(\mathbf{r}) = C\delta(\mathbf{r} - \mathbf{r}')u(\mathbf{r}), \quad (1)$$

where the boundary integral operators  $\mathcal{S}_{bi}$  and  $\mathcal{F}_{bi}$  are defined as

$$(\mathcal{S}_{bi}u)(\mathbf{r}) = \int_{\Gamma_{bi}} q(\mathbf{r}')G_b(\mathbf{r}, \mathbf{r}')dL', \quad (2)$$

$$(\mathcal{F}_{bi}u)(\mathbf{r}) = \int_{\Gamma_{bi}} u(\mathbf{r}')G_b^*(\mathbf{r}, \mathbf{r}')dL'. \quad (3)$$

For the transverse electric (TE) polarizations,  $u$  denotes the  $z$  component of the electric fields  $\mathbf{E}$ , and Eq. (1) is referred to as the electric field integral equation (EFIE). For the transverse magnetic polarizations,  $u$  denotes the  $z$  component of the magnetic fields  $\mathbf{H}$ , and Eq. (1) is referred to as the magnetic field integral equation (MFIE).  $\mathbf{r} = (x, y) \in \Gamma_b = \sum_{i=1}^L \Gamma_{bi}$  and  $\mathbf{r}' = (x', y') \in \Gamma_{bi}$ .  $\mathbf{r}$  and  $\mathbf{r}'$  denote the positions of the observation point and source point, respectively.  $q(\mathbf{r}') = \mathbf{n}_{bi}(\mathbf{r}') \cdot \nabla' u(\mathbf{r}')$ , where  $\mathbf{n}_{bi}(\mathbf{r}')$  is the unit normal at  $\mathbf{r}'$  pointing to the exterior region of  $\Omega_b$ .  $u^{\text{inc}}(\mathbf{r})$  is the incident field at  $\mathbf{r}$ . In this paper, we are interested in the scattering of a plane wave  $u^{\text{inc}}(\mathbf{r}) = u_0 e^{-jk\mathbf{d}_{\text{inc}} \cdot \mathbf{r}}$ , where  $u_0$  represents the amplitude of the incident wave, and  $\mathbf{d}_{\text{inc}} = (\cos \theta_{\text{inc}}, \sin \theta_{\text{inc}})$  with  $\theta_{\text{inc}} \in [0, 2\pi)$  representing the incident angle. The constant  $C = \beta/2\pi$ , where  $\beta$  is the exterior angle at  $\mathbf{r}'$ .  $\delta$  is the delta function, and  $G_b(\mathbf{r}, \mathbf{r}')$  represents the Green's function of the Helmholtz equation with wavenumber  $k_b = k_0 \sqrt{\epsilon_{r,b} \mu_{r,b}}$ , i.e.,

$$G_b(\mathbf{r}, \mathbf{r}') = \frac{1}{4j} H_0^{(2)}(k_b |\mathbf{r} - \mathbf{r}'|), \quad (4)$$

$$\begin{aligned} G_b^*(\mathbf{r}, \mathbf{r}') &= \mathbf{n}_{bi}(\mathbf{r}') \cdot \mathbf{grad}_{\mathbf{r}'} G_b(\mathbf{r}, \mathbf{r}') \\ &= \frac{jk_b}{4} H_1^{(2)}(k_b |\mathbf{r} - \mathbf{r}'|) \frac{\mathbf{n}_{bi}(\mathbf{r}') \cdot (\mathbf{r}' - \mathbf{r})}{|\mathbf{r} - \mathbf{r}'|}, \end{aligned} \quad (5)$$

where  $j$  is the imaginary unit, and  $k_0 = 2\pi/\lambda_0$  is the wavenumber corresponding to a free space wavelength  $\lambda_0$ .  $\epsilon_{r,b}$  and  $\mu_{r,b}$  are the relative permittivity and permeability, respectively, in  $\Omega_b$ .  $H_0^{(2)}(k_b |\mathbf{r} - \mathbf{r}'|)$  and  $H_1^{(2)}(k_b |\mathbf{r} - \mathbf{r}'|)$  are the zeroth- and first-order Hankel function of the second kind, respectively.

To solve Eq. (1), we first divide the boundary  $\Gamma_b$  into small segments with totally  $\mathcal{N}_b$  points, and approximate the undetermined  $u$  and  $q$  by a set of predefined basis functions. Multiplying Eq. (1) by a set of testing functions  $v_1(\mathbf{r}), \dots, v_{\mathcal{N}_b}(\mathbf{r})$  individually and integrating the products over the boundary  $\Gamma_b$ , Eq. (1) is then converted into a linear system with undetermined expansion coefficients of  $u$  and  $q$ . Note that the choice of testing functions is versatile, and the commonly used testing functions under the 2D formalism are the simple delta function, i.e.,  $v_m(\mathbf{r}) = \delta(\mathbf{r}_m - \mathbf{r})$ . Replacing  $\mathbf{r}$  in Eqs. (1)–(5) with  $\mathbf{r}_m$  yields the final weak form of the integral equation. Establishing the BIEs in all regions and further considering the boundary conditions, the boundary field  $u$  and its normal derivative  $q$  can be finally obtained by solving the linear system. Note that  $u^{\text{inc}}(\mathbf{r}) = 0$  in the region without a source.

In practice, the EFIE and MFIE may suffer from the interior resonance for a scatterer with a closed boundary. A remedy for this phenomenon is to combine EFIE and MFIE together. Since the main purpose of this paper is to demonstrate the combination of RBM with BIE, but not to introduce the best choice of BIE for modeling, for the sake of simplicity, we will describe RB-BEM based on the BIE in Eq. (1) by assuming that the resonance wavenumber has been removed from the considered parameter domain. It should be pointed out that the RB-BEM could be readily extended to other BIEs, such as the combined-field integral equation.

### B. 3D Electromagnetic Scattering Problem

The basic methodology for the 2D analysis can be extended to the analysis of 3D vector fields. For the sake of clarity, here we consider the problem of a vector wave produced by a source  $[\mathbf{E}^{\text{inc}}, \mathbf{H}^{\text{inc}}]$  in the presence of a homogeneous dielectric scatterer  $\Omega_2$ , which only consists of one boundary  $\Gamma$  immersed in a homogeneous medium  $\Omega_1$ . Note that this configuration could be readily extended to a piecewise homogeneous scatterer or multiple scatterers. The formulation proposed by Poggio and Miller [12], Chang and Harrington [15], and Wu and Tsai [13], which is often referred to as PMCHWT formulas,

$$\mathbf{n} \times [-\eta_1 \mathcal{L}_1(\mathbf{J}) + \mathcal{K}_1(\mathbf{M}) - \eta_2 \mathcal{L}_2(\mathbf{J}) + \mathcal{K}_2(\mathbf{M})] = \mathbf{n} \times \mathbf{E}^{\text{inc}}, \quad (6)$$

$$-\mathbf{n} \times [\mathcal{K}_1(\mathbf{J}) + \eta_1^{-1} \mathcal{L}_1(\mathbf{M}) + \mathcal{K}_2(\mathbf{J}) + \eta_2^{-1} \mathcal{L}_2(\mathbf{M})] = \mathbf{n} \times \mathbf{H}^{\text{inc}}, \quad (7)$$

is found to be free of interior resonance and yields accurate and stable solutions for modeling the electromagnetic scattering problem of a 3D dielectric scatterer. The boundary integral operators  $\mathcal{L}_b$  and  $\mathcal{K}_b$  in Eqs. (6) and (7) are defined as

$$\mathcal{L}_b(\mathbf{X}) = -jk_b \int_{\Gamma} [\mathbf{X}(\mathbf{r}') + k_b^{-2} \text{div}_{\mathbf{r}'} \mathbf{X}(\mathbf{r}') \mathbf{grad}_{\mathbf{r}'}] G_b(\mathbf{r}, \mathbf{r}') ds', \quad (8)$$

$$\mathcal{K}_b(\mathbf{X}) = - \int_{\Gamma} \mathbf{X}(\mathbf{r}') \times \mathbf{grad}_{\mathbf{r}'} G_b(\mathbf{r}, \mathbf{r}') ds', \quad b = 1, 2, \quad (9)$$

where the Green's function of the Helmholtz equation and its gradient are

$$G_b(\mathbf{r}, \mathbf{r}') = \frac{e^{-jk_b |\mathbf{r} - \mathbf{r}'|}}{4\pi |\mathbf{r} - \mathbf{r}'|}, \quad (10)$$

$$\mathbf{grad}_{\mathbf{r}'} G_b(\mathbf{r}, \mathbf{r}') = \frac{(1 + jk_b |\mathbf{r} - \mathbf{r}'|) e^{-jk_b |\mathbf{r} - \mathbf{r}'|}}{4\pi |\mathbf{r} - \mathbf{r}'|^3} (\mathbf{r}' - \mathbf{r}). \quad (11)$$

In Eqs. (6) and (7),  $\mathbf{J}$  and  $\mathbf{M}$  are the equivalent electric and magnetic currents on  $\Gamma$ , respectively,  $\mathbf{n}$  denotes the unit normal on  $\Gamma$  pointing from the interior of scatterer  $\Omega_2$  to the exterior  $\Omega_1$ , and  $\eta_b = \sqrt{\mu_{r,b}/\epsilon_{r,b}}$  is the wave impedance in  $\Omega_b$ .

Similarly, to solve the PMCHWT formulas, one needs to divide the boundary  $\Gamma$  into small patches, and test the discrete PMCHWT formulas by a set of testing functions. A common choice of the basis functions defined on the patches is the triangle rooftop functions [14], which are also known as the Rao–Wilton–Glisson (RWG) functions. In this case, the commonly used testing functions  $\mathbf{v}(\mathbf{r})$  are also RWG functions. Then the weak form of PMCHWT formulas can be written as

$$\sum_{b=1}^2 a_{1,b}(\mathbf{J}, \mathbf{v}) + \sum_{b=1}^2 a_{2,b}(\overline{\mathbf{M}}, \mathbf{v}) = f_{\mathbf{J}}(\mathbf{E}^{\text{inc}}, \mathbf{v}), \quad (12)$$

$$\sum_{b=1}^2 a_{3,b}(\mathbf{J}, \mathbf{v}) + \sum_{b=1}^2 a_{4,b}(\overline{\mathbf{M}}, \mathbf{v}) = f_{\overline{\mathbf{M}}}(\overline{\mathbf{H}}^{\text{inc}}, \mathbf{v}), \quad (13)$$

where

$$a_{1,b}(\mathbf{J}, \mathbf{v}) = jk_b \eta_b \mathcal{X}_b^1(\mathbf{J}, \mathbf{v}) - jk_b^{-1} \eta_b \mathcal{X}_b^2(\mathbf{J}, \mathbf{v}), \quad (14)$$

$$a_{2,b}(\overline{\mathbf{M}}, \mathbf{v}) = -\eta_0 \mathcal{Y}_b(\overline{\mathbf{M}}, \mathbf{v}), \quad (15)$$

$$a_{3,b}(\mathbf{J}, \mathbf{v}) = \eta_0 \mathcal{Y}_b(\mathbf{J}, \mathbf{v}), \quad (16)$$

$$a_{4,b}(\mathbf{J}, \mathbf{v}) = jk_b \eta_0^2 \eta_b^{-1} \mathcal{X}_b^1(\overline{\mathbf{M}}, \mathbf{v}) - jk_b^{-1} \eta_0^2 \eta_b^{-1} \mathcal{X}_b^2(\overline{\mathbf{M}}, \mathbf{v}), \quad (17)$$

$$f_{\mathbf{E}^{\text{inc}}}(\mathbf{v}) = \int_{\Gamma} \mathbf{v}(\mathbf{r}) \cdot \mathbf{E}^{\text{inc}}(\mathbf{r}) ds, \quad (18)$$

$$f_{\overline{\mathbf{H}}^{\text{inc}}}(\mathbf{v}) = \int_{\Gamma} \mathbf{v}(\mathbf{r}) \cdot \overline{\mathbf{H}}^{\text{inc}}(\mathbf{r}) ds. \quad (19)$$

The boundary integral operators  $\mathcal{X}_b^1$ ,  $\mathcal{X}_b^2$ , and  $\mathcal{Y}_b$  are defined as

$$\mathcal{X}_b^1(\mathbf{X}, \mathbf{v}) = \int_{\Gamma} \int_{\Gamma} \mathbf{v}(\mathbf{r}) \cdot \mathbf{X}(\mathbf{r}') G_b(\mathbf{r}, \mathbf{r}') ds' ds, \quad (20)$$

$$\mathcal{X}_b^2(\mathbf{X}, \mathbf{v}) = \int_{\Gamma} \int_{\Gamma} \text{div}_{\mathbf{r}'} \mathbf{X}(\mathbf{r}') \text{div}_{\mathbf{r}} \mathbf{v}(\mathbf{r}) G_b(\mathbf{r}, \mathbf{r}') ds' ds, \quad (21)$$

$$\mathcal{Y}_b(\mathbf{X}, \mathbf{v}) = \int_{\Gamma} \int_{\Gamma} \mathbf{v}(\mathbf{r}) \cdot [\mathbf{X}(\mathbf{r}') \times \mathbf{grad}_{\mathbf{r}'} G_b(\mathbf{r}, \mathbf{r}')] ds' ds. \quad (22)$$

Here,  $\eta_0 = \sqrt{\mu_0/\epsilon_0}$  is the wave impedance in free space, and  $\epsilon_0$  and  $\mu_0$  are the permittivity and permeability in free space, respectively.  $\overline{\mathbf{M}} = \eta_0^{-1}\mathbf{M}$  and  $\overline{\mathbf{H}}^{\text{inc}} = \eta_0\mathbf{H}^{\text{inc}}$ , which are introduced to ensure the numerical stability. The incident electric field  $\mathbf{E}^{\text{inc}}$  is defined as  $\mathbf{E}^{\text{inc}}(\mathbf{r}) = A\mathbf{p}_E^{\text{inc}}e^{jk\mathbf{d}_{\text{inc}}\cdot\mathbf{r}}$ , with  $A$  representing the amplitude of the electric field,  $\mathbf{d}_{\text{inc}} = -(\sin\theta_{\text{inc}}\cos\varphi_{\text{inc}}, \sin\theta_{\text{inc}}\sin\varphi_{\text{inc}}, \cos\theta_{\text{inc}})$ ,  $\theta_{\text{inc}} \in [0, \pi]$ , and  $\varphi_{\text{inc}} \in [0, 2\pi)$ , denoting the incident angles in the spherical coordinate;  $\mathbf{p}_E^{\text{inc}}$  represents the polarization direction of the electric field,  $\overline{\mathbf{H}}^{\text{inc}}(\mathbf{r}) = A\mathbf{p}_H^{\text{inc}}e^{jk\mathbf{d}_{\text{inc}}\cdot\mathbf{r}}$ , and  $\mathbf{p}_H^{\text{inc}} = \mathbf{d}_{\text{inc}} \times \mathbf{p}_E^{\text{inc}}$ . Finally, we can obtain the expansion coefficients of  $\mathbf{J}$  and  $\overline{\mathbf{M}}$  by solving the linear system given in Eqs. (12) and (13).

For clarity, in the following parts of this work, the subscript  $h$  in Eqs. (1)–(5) and (8)–(22) used to indicate the homogenous region will be omitted. Note also that our method is not constrained to the specific type of incident field. In this section, the reason we specify the form of incident field is just for the convenience of description.

To intuitively present the output signal of a 3D scattering problem, we introduce the radar cross section (RCS) denoted by  $\sigma$  as an indicator of the far field [33]:

$$\sigma(\mathbf{J}, \mathbf{d}_{\text{rcs}}) = 10 \log_{10}(4\pi|\mathbf{E}^{\infty}(\mathbf{J}, \mathbf{d}_{\text{rcs}})|^2/|\mathbf{E}^{\text{inc}}|^2), \quad (23)$$

where the electric far field  $\mathbf{E}^{\infty}$  is defined as

$$\mathbf{E}^{\infty}(\mathbf{J}, \mathbf{d}_{\text{rcs}}) = \frac{jk_0\eta_0}{4\pi} \int_{\Gamma} \mathbf{d}_{\text{rcs}} \times (\mathbf{J}(\mathbf{r}') \times \mathbf{d}_{\text{rcs}}) e^{jk_0\mathbf{d}_{\text{rcs}}\cdot\mathbf{r}'} d\mathbf{s}' \quad (24)$$

for a given unit directional vector  $\mathbf{d}_{\text{rcs}}$ :

$$\mathbf{d}_{\text{rcs}} = (\sin\theta_{\text{rcs}}\cos\varphi_{\text{rcs}}, \sin\theta_{\text{rcs}}\sin\varphi_{\text{rcs}}, \cos\theta_{\text{rcs}}), \quad (25)$$

with  $\theta_{\text{rcs}} \in [0, \pi]$  and  $\varphi_{\text{rcs}} \in [0, 2\pi)$  denoting the observation angles in the spherical coordinate.

### 3. REDUCED-BASIS METHOD

In this section, we will first introduce the key points in RBM, including the dimensional reduction of the high-dimensional BEM model and the offline–online decomposition of the computational effort. Then improved greedy algorithms are introduced to decrease the work load in the offline phase.

#### A. Principle of RBM

In the parameterized context, the modeling of a electromagnetic scattering problem finally comes down to finding the solution of a parameterized linear system, i.e., for any  $\mu \in \mathcal{D}$ , find  $\psi \in \mathbb{W}_{\mathcal{N}}$  such that

$$a(\psi, \mathbf{v}; \mu) = f(\mathbf{v}; \mu), \quad \forall \mathbf{v} \in \mathbb{W}_{\mathcal{N}}, \quad (26)$$

where  $\psi$  is the unknown quantity and  $\mathbf{v}$  is the testing function. The symbol  $\mu$  denotes the variable parameters, which may be the characteristic parameters of the incident field such as the wavelength and incident angle, the geometric parameters of the scatterer, or the observation angles of the far-field pattern.  $\mathcal{D}$  is the parameter domain, and  $\mathbb{W}_{\mathcal{N}}$  denotes the finite dimensional boundary element space with a dimension of  $\mathcal{N}$ . Writing the original model obtained by BEM into a matrix form, we have

$$\mathbf{A}(\mu)\mathbf{x}(\mu) = \mathbf{b}(\mu), \quad (27)$$

where the  $\mathcal{N} \times \mathcal{N}$  matrix  $\mathbf{A}$  is known as the impedance matrix,  $\mathbf{x}$  represents the undetermined quantities, and  $\mathbf{b}$  is the excitation

term. Generally, the boundary of a scatterer is decomposed into a lot of segments or patches to get solutions with high accuracy. Therefore, calculating the entities of matrix  $\mathbf{A}$ , as well as finding the solution of Eq. (27), are both time-consuming, especially in the parameterized context.

Assume that we have obtained a reduced basis space  $\mathbb{W}_N = \text{span}\{\boldsymbol{\psi}(\boldsymbol{\mu}_n)\}$ ,  $n = 1, \dots, N$ ,  $N \ll \mathcal{N}$ , and a set of chosen parameter snapshots  $\mathbb{S}_N = \{\boldsymbol{\mu}_n\}_{n=1}^N$ . The reduced-basis approximation of the original model is defined as follows: for any  $\mu \in \mathcal{D}$ , find  $\boldsymbol{\psi}_N \in \mathbb{W}_N$  such that [23–27]

$$a(\boldsymbol{\psi}_N, \mathbf{v}_N; \mu) = f(\mathbf{v}_N; \mu), \quad \forall \mathbf{v}_N \in \mathbb{W}_N. \quad (28)$$

The parameter set  $\mathbb{S}_N$  is chosen by the greedy algorithm, which will be discussed in Section 3.B in detail. Note that, in order to obtain a well-conditioned reduced-basis model, the basis function should be orthogonal, i.e.,  $\mathbb{W}_N = \text{span}\{\boldsymbol{\xi}_n\}$ ,  $n = 1, \dots, N$ , with  $\boldsymbol{\xi}_m \cdot \boldsymbol{\xi}_n = \delta_{mn}$ . Therefore, the reduced-basis model can be regarded as the Galerkin projection result of the original model into the reduced-basis space  $\mathbb{W}_N$ . Although solving the low-dimensional reduced-basis model will be intuitively much faster than directly solving the high-dimensional original model, there still exists another issue that restricts the computational efficiency of the reduced-basis model. To be specific, we need to obtain the original model for  $\forall \mu \in \mathcal{D}$  before projecting it into the reduced-basis space to further obtain the reduced-basis model.

To address this issue, we assume that both the bilinear form  $a(\cdot, \cdot; \mu)$  and the linear form  $f(\cdot; \mu)$  in Eq. (28) satisfy the affine decomposition assumption. Under this assumption, the original parameter-dependent forms can be decomposed into a finite sum of parameter-dependent scalar functions multiplied by parameter-independent forms as follows:

$$a(\cdot, \cdot; \mu) = \sum_{m=1}^{M_a} a^m(\cdot, \cdot) \Theta_a^m(\mu), \quad (29)$$

$$f(\cdot; \mu) = \sum_{m=1}^{M_f} f^m(\cdot) \Theta_f^m(\mu). \quad (30)$$

The parameter affine assumption is the basis of the offline–online decomposition of the computational effort. However, we should point out that, in many practical applications such as the BIEs introduced in Section 2, the parameter affine assumption may not be satisfied naturally. To this end, a method called EIM [33,34] is often used to approximately construct the expressions in Eqs. (29) and (30). Based on this assumption, instead of reducing the parameter-dependent forms  $a(\cdot, \cdot; \mu)$  and  $f(\cdot; \mu)$  for  $\forall \mu \in \mathcal{D}$ , we only need to reduce the parameter-independent forms  $a^m(\cdot, \cdot)$  and  $f^m(\cdot)$  one time. Then the reduced-basis model can be obtained through the linear assembly of the reduced forms, where the coefficients  $\Theta_a^m(\mu)$  and  $\Theta_f^m(\mu)$  are the solutions of linear systems with dimensions of  $M_a$  and  $M_f$ , respectively. Therefore, the solution of Eq. (28) is efficient since the input–output procedure is now independent of the dimension of the original model. Similarly, to improve the efficiency of calculating output signal  $s(\cdot; \mu)$  for  $\forall \mu \in \mathcal{D}$ , such as the RCS signal in our cases, it can be written as

$$s(\cdot; \boldsymbol{\mu}) = \sum_{m=1}^{M_s} s^m(\cdot) \Theta_s^m(\boldsymbol{\mu}). \quad (31)$$

In summary, in the offline phase of RBM, the computational effort consists of the following:

- (1) dividing the parameter-dependent forms  $a(\cdot; \boldsymbol{\mu})$ ,  $f(\cdot; \boldsymbol{\mu})$ , and  $s(\cdot; \boldsymbol{\mu})$  into a finite sum of parameter-dependent scalar functions multiplied by parameter-independent forms;
- (2) constructing the reduced-basis space, and reducing the dimension of parameter-independent forms  $a^m(\cdot, \cdot)$  and  $f^m(\cdot)$ .

In the online phase, the computational effort consists of the following:

- (1) calculating parameter-dependent scalar functions  $\Theta_a^m(\boldsymbol{\mu})$ ,  $\Theta_f^m(\boldsymbol{\mu})$ , and  $\Theta_s^m(\boldsymbol{\mu})$  for  $\forall \boldsymbol{\mu} \in \mathcal{D}$ ;
- (2) using data from the offline phase to construct the reduced-basis model, and finding solutions for  $\forall \boldsymbol{\mu} \in \mathcal{D}$ .

Since the computational effort in the online phase only depends on the dimension of the affine decomposition expression and the dimension of the reduced-basis model, the computational efficiency is thereby expected to be dramatically improved in comparison with direct solution of the original model.

## B. Improved Greedy Algorithm

The greedy algorithm plays a very important role in constructing the reduced-basis space and realizing the affine decomposition of parameter-dependent forms using EIM. The typical procedure of a standard greedy algorithm [25] is as follows:

**Step 1:** selecting a finite dimensional training set  $\Xi \in \mathcal{D}$ , and randomly picking a  $\boldsymbol{\mu}^1 \in \Xi$ ; then  $\mathbb{S}_1 = \{\boldsymbol{\mu}^1\}$ ,  $\mathbb{W}_1 = \text{span}\{\boldsymbol{\xi}(\boldsymbol{\mu}^1)\}$ , where  $\boldsymbol{\xi}$  is the solution of original model, or a parameter-dependent function defined on some specific space points; set  $N = 1$ ;

**Step 2:** computing the error indicator  $\varepsilon_N(\boldsymbol{\mu})$  for all  $\boldsymbol{\mu} \in \Xi$ , and selecting the next parameter snapshot  $\boldsymbol{\mu}^{N+1} = \text{argmax}_{\boldsymbol{\mu} \in \Xi} \varepsilon_N(\boldsymbol{\mu})$ ;

**Step 3:**  $\mathbb{S}_{N+1} = \mathbb{S}_N \cup \{\boldsymbol{\mu}^{N+1}\}$ ,  $\mathbb{W}_{N+1} = \mathbb{W}_N \cup \{\boldsymbol{\xi}(\boldsymbol{\mu}^{N+1})\}$ ,  $N \leftarrow N + 1$ .

Steps 2 and 3 are repeated until the error indicator  $\varepsilon_N(\boldsymbol{\mu})$  is smaller than a prescribed tolerance  $\text{tol}$  for all  $\boldsymbol{\mu} \in \Xi$ , or  $N \geq N_{\max}$ , where  $N_{\max}$  is a prescribed number of maximum iterations. When the greedy algorithm is used to realize the affine decomposition of parameter-dependent function, the error indicator  $\varepsilon_N(\boldsymbol{\mu})$  could be the 2-norm of the relative error vector between the function and its affine decomposition expression with totally  $N$  terms. When constructing the reduced-basis space by the greedy algorithm, the error indicator is defined as

$$\varepsilon_N(\boldsymbol{\mu}) = \|\mathbf{x}(\boldsymbol{\mu}) - \mathbf{x}_N^{\text{rb}}(\boldsymbol{\mu})\|_2 / \|\mathbf{x}(\boldsymbol{\mu})\|_2, \quad (32)$$

where  $\mathbf{x}_N^{\text{rb}}(\boldsymbol{\mu})$  is the vectorial representation of the solution of a  $N$ -dimensional reduced-basis model in the boundary element space  $\mathbb{W}_N$ .

From this description, we notice that the training set  $\Xi$  should be large enough to guarantee the approximate accuracy of  $\mathbb{W}_N$  for  $\forall \boldsymbol{\mu} \in \mathcal{D}$ . However, such a large  $\Xi$  will result in huge computational cost, especially in high-dimensional  $\mathcal{D}$ , since the computational effort in Step 2 linearly depends on the size of  $\Xi$ .

To address this problem, Hesthaven *et al.* [37] proposed an improved greedy algorithm based on a saturation assumption. Specifically, the error indicator  $\varepsilon_N(\boldsymbol{\mu})$  is expected to satisfy the saturation assumption

$$\varepsilon_M(\boldsymbol{\mu}) \leq C_{\text{sa}} \varepsilon_N(\boldsymbol{\mu}) \quad (33)$$

for all  $M > N > 0$  with a  $C_{\text{sa}} > 0$ , since  $\varepsilon_N(\boldsymbol{\mu})$  always presents an exponential convergence property with the increase of  $N$ . Based on this saturation assumption, a snapshot is selected from those parameters that cannot satisfy the saturation assumption. Therefore, compared to the standard greedy algorithm, the computational effort in Step 2 is reduced in the improved greedy algorithm. In Eq. (33),  $C_{\text{sa}}$  is a critical parameter that determines the efficiency of the improved greedy algorithm, whose value cannot be chosen freely, and  $C_{\text{sa}} = 2$  is a typically recommended value [37].

Instead of constructing an approximate space based on a large enough training set, as the standard greedy algorithm and the improved algorithm based on the saturation assumption did, we propose an improved greedy algorithm on multi-grid. In the proposed algorithm, we first select multiple training sets with increasing sizes from  $\mathcal{D}$ , and then recursively train the approximate space on these sets. In other words, the approximate space obtained from a coarse set will be further trained on a finer set. Since the approximate space is rapidly constructed on the coarse sets and remedied on the fine set, the computational cost is expected to be further reduced in comparison with the improved greedy algorithm based on the saturation assumption.

Hereinafter, for the sake of clarity, we denote the standard greedy algorithm, improved greedy algorithm based on saturation assumption, and improved greedy algorithm on multi-grid as Methods 1, 2, and 3, respectively. To further improve the efficiency of the greedy algorithm, the saturation assumption on all the training sets can also be applied in Method 3. The hybrid method combining Method 3 and the saturation assumption is termed Method 4.

## 4. REDUCED-BASIS BOUNDARY ELEMENT METHOD

In many applications, such as measurement and optimal design, the geometric profile of a scatterer is an important target to be measured or optimized. To avoid repeatedly partitioning the boundary of a physical scatterer in the parameterized context, the best choice is first defining a reference scatterer, then constructing a transformation operator  $\mathcal{T}: \hat{\Gamma} \rightarrow \Gamma$  from the boundary of the reference scatterer to a physical one. The operator has a specific form as  $\mathcal{T}(\hat{\mathbf{r}}) = \gamma \mathcal{R} \hat{\mathbf{r}} + \mathbf{t}$ , where  $\hat{\mathbf{r}}$  is the position vector of a point on the reference boundary  $\hat{\Gamma}$ ,  $\gamma \in \mathbb{R}$  is the scaling factor,  $\mathcal{R} \in \mathbb{R}^{d \times d}$  is the rotation matrix, and  $\mathbf{t} \in \mathbb{R}^{d \times 1}$  is the translation vector, where  $d = 2, 3$  denotes the dimension of the problem under study. The Piola transformation operator  $\hat{\mathcal{P}}$  [34] of a vector  $\boldsymbol{\rho}$  from the physical boundary to the reference one is defined as

$$(\hat{\mathcal{P}}\boldsymbol{\rho})(\hat{\mathbf{r}}) := \mathcal{R}^T \boldsymbol{\rho}(\mathcal{T}(\hat{\mathbf{r}})), \quad (34)$$

where the superscript “ $T$ ” denotes matrix transpose. Next, we will introduce how to combine the RBM with BEM for

efficient modeling of 2D and 3D electromagnetic scattering problems.

### A. 2D Electromagnetic Scattering Problem

To model the 2D electromagnetic scattering problems, first we map the BIE in Eq. (1) to the reference boundary  $\hat{\Gamma}$ . Letting  $\mathbf{r} = \mathcal{T}(\hat{\mathbf{r}})$  and  $\mathbf{r}' = \mathcal{T}'(\hat{\mathbf{r}}')$  in Eq. (1), we have

$$\hat{u}^{\text{inc}}(\hat{\mathbf{r}}; \boldsymbol{\mu}) + \sum_{i=1}^I (\hat{\mathcal{S}}_i u)(\hat{\mathbf{r}}; \boldsymbol{\mu}) - (\hat{\mathcal{F}}_i u)(\hat{\mathbf{r}}; \boldsymbol{\mu}) = C \hat{\delta}(\hat{\mathbf{r}}, \hat{\mathbf{r}}'; \boldsymbol{\mu}) \hat{u}(\hat{\mathbf{r}}), \quad (35)$$

where

$$(\hat{\mathcal{S}}_i \hat{u})(\hat{\mathbf{r}}; \boldsymbol{\mu}) = \gamma' \int_{\hat{\Gamma}_i} \hat{q}(\hat{\mathbf{r}}') \hat{G}(\hat{\mathbf{r}}, \hat{\mathbf{r}}'; \boldsymbol{\mu}) d\mathbf{l}', \quad (36)$$

$$(\hat{\mathcal{F}}_i \hat{u})(\hat{\mathbf{r}}; \boldsymbol{\mu}) = \gamma' \int_{\hat{\Gamma}_i} \hat{u}(\hat{\mathbf{r}}') \hat{G}^*(\hat{\mathbf{r}}, \hat{\mathbf{r}}'; \boldsymbol{\mu}) d\mathbf{l}', \quad (37)$$

$$\hat{u}^{\text{inc}}(\hat{\mathbf{r}}; \boldsymbol{\mu}) = u^{\text{inc}}(\mathcal{T}(\hat{\mathbf{r}})), \quad (38)$$

$$\hat{\delta}(\hat{\mathbf{r}}, \hat{\mathbf{r}}'; \boldsymbol{\mu}) = \delta(\mathcal{T}(\hat{\mathbf{r}}) - \mathcal{T}'(\hat{\mathbf{r}}')). \quad (39)$$

The Green's function and its normal derivative defined on  $\hat{\Gamma}$  are

$$\hat{G}(\hat{\mathbf{r}}, \hat{\mathbf{r}}'; \boldsymbol{\mu}) = G(\mathcal{T}(\hat{\mathbf{r}}), \mathcal{T}'(\hat{\mathbf{r}}')), \quad (40)$$

$$\hat{G}^*(\hat{\mathbf{r}}, \hat{\mathbf{r}}'; \boldsymbol{\mu}) = \frac{jk}{4} H_1^{(2)}(k|\mathcal{T}(\hat{\mathbf{r}}) - \mathcal{T}'(\hat{\mathbf{r}}')|) \times \frac{\mathcal{R} \hat{\mathbf{n}}_i(\hat{\mathbf{r}}') \cdot (\mathcal{T}'(\hat{\mathbf{r}}') - \mathcal{T}(\hat{\mathbf{r}}))}{|\mathcal{T}'(\hat{\mathbf{r}}') - \mathcal{T}(\hat{\mathbf{r}})|}, \quad (41)$$

where  $\hat{\mathbf{n}}_i(\hat{\mathbf{r}}') = (\hat{\mathcal{P}} \mathbf{n}_i)(\hat{\mathbf{r}}')$  is the unit normal on  $\hat{\Gamma}_i$ .  $\hat{u}(\hat{\mathbf{r}}) = u(\mathcal{T}(\hat{\mathbf{r}}))$  and  $\hat{q}(\hat{\mathbf{r}}') = q(\mathcal{T}'(\hat{\mathbf{r}}'))$  are the unknowns on the physical boundary. Note that the transformation defined by  $\mathcal{T}$  is a kind of topological transformation, which means that  $\mathbf{r}_1 \neq \mathbf{r}_2$  if  $\hat{\mathbf{r}}_1 \neq \hat{\mathbf{r}}_2$ . Therefore, the operator  $\mathcal{T}$  has no effect on the delta function, i.e.,  $\hat{\delta}(\hat{\mathbf{r}}, \hat{\mathbf{r}}'; \boldsymbol{\mu}) = \delta(\hat{\mathbf{r}} - \hat{\mathbf{r}}')$ .

Next, we need to construct the affine decomposition expressions for parameter-dependent functions by using EIM. Note that the premise of EIM is that the approximated function is smooth enough on  $\mathcal{Q} \times \mathcal{D}$ , where  $\mathcal{Q}$  denotes the spatial domain and  $\mathcal{D}$  denotes the parameter domain. However, the second term on the right side of Eq. (41), which physically means the included angle between the unit normal  $\mathbf{n}_i(\mathbf{r}')$  and the spatial vector  $\mathbf{r}' - \mathbf{r}$ , is usually not smooth. The affine decomposition expression of  $\hat{u}^{\text{inc}}(\hat{\mathbf{r}}; \boldsymbol{\mu})$  is

$$\mathcal{I}(\hat{u}^{\text{inc}})(\hat{\mathbf{r}}; \boldsymbol{\mu}) = \sum_{m=1}^{M^{\text{inc}}} \alpha_m^{\text{inc}}(\boldsymbol{\mu}) \phi_m^{\text{inc}}(\hat{\mathbf{r}}). \quad (42)$$

The process of constructing affine decomposition expressions for  $\hat{G}(\hat{\mathbf{r}}, \hat{\mathbf{r}}'; \boldsymbol{\mu})$  and/or its normal derivative can be classified into two different cases:

*Case 1.  $\mathcal{T} = \mathcal{T}'$*

In this case, considering the small argument approximations, the Hankel function  $\hat{H}_0^{(2)}(\hat{\mathbf{r}}, \hat{\mathbf{r}}'; \boldsymbol{\mu})$  and  $\hat{H}_1^{(2)}(\hat{\mathbf{r}}, \hat{\mathbf{r}}'; \boldsymbol{\mu})$  can be decomposed into the summation of a non-singular part (denoted by superscript "ns") and a singular part,

$$\hat{H}_0^{(2)}(\hat{\mathbf{r}}, \hat{\mathbf{r}}'; \boldsymbol{\mu}) = \hat{H}_0^{(2),\text{ns}}(\hat{\mathbf{r}}, \hat{\mathbf{r}}'; \boldsymbol{\mu}) - \frac{2j}{\pi} \ln \frac{\gamma k |\hat{\mathbf{r}}_0|}{2}, \quad (43)$$

$$\hat{H}_1^{(2)}(\hat{\mathbf{r}}, \hat{\mathbf{r}}'; \boldsymbol{\mu}) = \hat{H}_1^{(2),\text{ns}}(\hat{\mathbf{r}}, \hat{\mathbf{r}}'; \boldsymbol{\mu}) + \frac{2j}{\pi \gamma k} \frac{1}{|\hat{\mathbf{r}}_0|}, \quad (44)$$

where  $\hat{\mathbf{r}}_0 = \hat{\mathbf{r}}' - \hat{\mathbf{r}}$ . Note that  $\hat{H}_0^{(2),\text{ns}}(\hat{\mathbf{r}}, \hat{\mathbf{r}}'; \boldsymbol{\mu})$  and  $\hat{H}_1^{(2),\text{ns}}(\hat{\mathbf{r}}, \hat{\mathbf{r}}'; \boldsymbol{\mu})$  have no singularities when  $\hat{\mathbf{r}} \rightarrow \hat{\mathbf{r}}'$ , and can be decomposed by EIM as

$$\mathcal{I}(\hat{H}_0^{(2),\text{ns}})(\hat{\mathbf{r}}, \hat{\mathbf{r}}'; \boldsymbol{\mu}) = \sum_{m=1}^{M_0^{\text{ns}}} \alpha_{0,m}^{\text{ns}}(\boldsymbol{\mu}) \phi_{0,m}^{\text{ns}}(\hat{\mathbf{r}}, \hat{\mathbf{r}}'), \quad (45)$$

$$\mathcal{I}(\hat{H}_1^{(2),\text{ns}})(\hat{\mathbf{r}}, \hat{\mathbf{r}}'; \boldsymbol{\mu}) = \sum_{m=1}^{M_1^{\text{ns}}} \alpha_{1,m}^{\text{ns}}(\boldsymbol{\mu}) \phi_{1,m}^{\text{ns}}(\hat{\mathbf{r}}, \hat{\mathbf{r}}'). \quad (46)$$

Substituting Eqs. (45) and (46) into Eqs. (43) and (44), the Green's function and its normal derivative can be written as

$$\mathcal{I}(\hat{G})(\hat{\mathbf{r}}, \hat{\mathbf{r}}'; \boldsymbol{\mu}) = \frac{1}{4j} \sum_{m=-1}^{M_0^{\text{ns}}} \alpha_{0,m}^{\text{ns}}(\boldsymbol{\mu}) \phi_{0,m}^{\text{ns}}(\hat{\mathbf{r}}, \hat{\mathbf{r}}'), \quad (47)$$

$$\mathcal{I}(\hat{G}^*)(\hat{\mathbf{r}}, \hat{\mathbf{r}}'; \boldsymbol{\mu}) = \frac{j}{4} \sum_{m=0}^{M_1^{\text{ns}}} k \alpha_{1,m}^{\text{ns}}(\boldsymbol{\mu}) \phi_{1,m}^{\text{ns}}(\hat{\mathbf{r}}, \hat{\mathbf{r}}') \hat{\rho}_i. \quad (48)$$

In which  $\phi_{0,0}^{\text{ns}}(\hat{\mathbf{r}}, \hat{\mathbf{r}}') = (2j \ln |\hat{\mathbf{r}}_0|)/\pi$ ,  $\phi_{0,-1}^{\text{ns}}(\hat{\mathbf{r}}, \hat{\mathbf{r}}') = 2j/\pi$ ,  $\alpha_{0,0}^{\text{ns}}(\boldsymbol{\mu}) = -1$ ,  $\alpha_{0,-1}^{\text{ns}}(\boldsymbol{\mu}) = -\ln(\gamma k/2)$ ,  $\phi_{1,0}^{\text{ns}}(\hat{\mathbf{r}}, \hat{\mathbf{r}}') = 1/|\hat{\mathbf{r}}_0|$ ,  $\alpha_{0,-1}^{\text{ns}}(\boldsymbol{\mu}) = -1/(2\pi\gamma)$ , and  $\hat{\rho}_i = \hat{\mathbf{n}}_i(\hat{\mathbf{r}}') \cdot \hat{\mathbf{r}}_0/|\hat{\mathbf{r}}_0|$ .

Substituting Eqs. (47) and (48) into Eqs. (36) and (37), the integration about  $\phi_{0,m}^{\text{ns}}(\hat{\mathbf{r}}, \hat{\mathbf{r}}')$  and  $\phi_{1,m}^{\text{ns}}(\hat{\mathbf{r}}, \hat{\mathbf{r}}') \hat{\rho}_i$  can be calculated in the offline phase. We then project the obtained matrices and the parameter-independent excitation vectors  $\phi_m^{\text{inc}}(\hat{\mathbf{r}})$  into the reduced-basis space, and store these reduced matrices and vectors at the end of the offline phase. Therefore, in the online phase, for  $\forall \boldsymbol{\mu} \in \mathcal{D}$ , we only need to calculate the parameter-dependent coefficients in Eqs. (42), (47), and (48); then the reduced-basis model can be rapidly assembled using the stored reduced matrices and vectors.

*Case 2.  $\mathcal{T} \neq \mathcal{T}'$*

In this case,  $\hat{\mathbf{r}}$  and  $\hat{\mathbf{r}}'$  have different transformation operators, which indicates that they are located on two different boundaries, and the singularity in  $\hat{G}(\hat{\mathbf{r}}, \hat{\mathbf{r}}'; \boldsymbol{\mu})$  and  $\hat{G}^*(\hat{\mathbf{r}}, \hat{\mathbf{r}}'; \boldsymbol{\mu})$  cannot be separated analytically like what we did in Eqs. (43) and (44). Furthermore, the second term at the right side of Eq. (41) cannot be simplified as  $\hat{\rho}_i$ , i.e., this term is a parameter-dependent term. As mentioned previously, this term is the included angle between  $\mathbf{n}_j(\mathbf{r}')$  and  $\mathbf{r}' - \mathbf{r}$ , which are usually not a smooth function. Therefore,  $\hat{G}^*(\hat{\mathbf{r}}, \hat{\mathbf{r}}'; \boldsymbol{\mu})$  is also not a smooth function, and cannot be expressed into an affine decomposition form using EIM. In other words, the parameter-dependent integral in Eq. (37) has to be calculated and projected into reduced-basis space in the online phase, which will reduce the efficiency of RB-BEM.

Now we focus on the affine decomposition of the integral in Eq. (36). Let us denote the argument of the Hankel function as  $\omega$  (here  $\omega = k|\mathbf{r} - \mathbf{r}'|$ ) for simplicity; there exists a constant  $\tau$ , which makes  $H_0^{(2)}(\omega)$  non-singular for all  $\omega \geq \tau$ . According to the property of the Hankel function [38], the value of  $\tau$  is recommended to be 0.02 since, in this case,  $H_0^{(2)}(\omega)$  is

non-singular for all  $\omega \geq 0.02$ , and meanwhile the singular region  $\omega < 0.02$  of  $H_0^{(2)}(\omega)$  is not quite large either. Select those  $\hat{\mathbf{r}} \in \hat{\Gamma}$  and  $\hat{\mathbf{r}}' \in \hat{\Gamma}'$  satisfying  $k|\mathcal{T}(\mathbf{r}) - \mathcal{T}'(\mathbf{r}')| \geq \tau$  for  $\forall \boldsymbol{\mu} \in \mathcal{D}$ , and denote the sets of such  $\hat{\mathbf{r}}$  and  $\hat{\mathbf{r}}'$  as  $\hat{\Lambda}$  and  $\hat{\Lambda}'$ , respectively. Then the affine decomposition expression of  $\hat{H}_0^{(2)}(\hat{\mathbf{r}}, \hat{\mathbf{r}}'; \boldsymbol{\mu})$  can be written as

$$\mathcal{I}(\hat{H}_0^{(2)})(\hat{\mathbf{r}}, \hat{\mathbf{r}}'; \boldsymbol{\mu}) = \sum_{m=1}^{M_0} \alpha_{0,m}(\boldsymbol{\mu}) \phi_{0,m}(\hat{\mathbf{r}}, \hat{\mathbf{r}}'), \quad \hat{\mathbf{r}} \in \hat{\Lambda}, \quad \hat{\mathbf{r}}' \in \hat{\Lambda}'. \quad (49)$$

Similarly, substituting Eq. (49) into Eq. (36), the integration about  $\phi_{0,m}(\hat{\mathbf{r}}, \hat{\mathbf{r}}')$  can be calculated in the offline phase. Then the matrices obtained from integration can be projected into the reduced-basis space to obtain the corresponding parts of the reduced-basis model. Denote the complement set of  $\hat{\Lambda}$  in  $\hat{\Gamma}$  as  $\hat{\Gamma}/\hat{\Lambda}$ , and the complement set of  $\hat{\Lambda}'$  in  $\hat{\Gamma}'$  as  $\hat{\Gamma}'/\hat{\Lambda}'$ . For  $\hat{\mathbf{r}} \in \hat{\Gamma}/\hat{\Lambda}$  and  $\hat{\mathbf{r}}' \in \hat{\Gamma}'/\hat{\Lambda}'$ ,  $\exists \boldsymbol{\mu}$  makes  $k|\mathcal{T}(\mathbf{r}) - \mathcal{T}'(\mathbf{r}')| < \tau$ . Therefore, for these  $\hat{\mathbf{r}}$  and  $\hat{\mathbf{r}}'$ , the integral in Eq. (36) could also only be calculated and projected into reduced-basis space in the online phase. Generally, the size of  $(\hat{\Gamma}/\hat{\Lambda}) \cup (\hat{\Gamma}'/\hat{\Lambda}')$  is far smaller than that of  $\hat{\Lambda} \cup \hat{\Lambda}'$  with a proper  $\tau$ , such as what we mentioned above  $\tau = 0.02$ . Therefore, the computational cost related to  $\hat{\mathbf{r}} \in \hat{\Gamma}/\hat{\Lambda}$  and  $\hat{\mathbf{r}}' \in \hat{\Gamma}'/\hat{\Lambda}'$  will not dramatically increase the workload of the online phase.

### B. 3D Electromagnetic Scattering Problem

Similar to modeling the parameterized 2D electromagnetic scattering problem, first we need to map the BIEs in Eqs. (12) and (13) onto the reference boundary  $\hat{\Gamma}$ . Then the boundary integral operators in Eqs. (20)–(22) can be written as

$$\hat{\chi}^1(\hat{\mathbf{X}}, \hat{\mathbf{v}}; \boldsymbol{\mu}) = \gamma\gamma' \int_{\hat{\Gamma}} \int_{\hat{\Gamma}'} (\mathcal{R}\hat{\mathbf{v}}(\hat{\mathbf{r}})) \cdot (\mathcal{R}'\hat{\mathbf{X}}(\hat{\mathbf{r}}')) \hat{G}(\hat{\mathbf{r}}, \hat{\mathbf{r}}'; \boldsymbol{\mu}) ds' ds, \quad (50)$$

$$\hat{\chi}^2(\hat{\mathbf{X}}, \hat{\mathbf{v}}; \boldsymbol{\mu}) = \int_{\hat{\Gamma}} \int_{\hat{\Gamma}'} \text{div}_{\hat{\mathbf{r}}'} \hat{\mathbf{X}}(\hat{\mathbf{r}}') \text{div}_{\hat{\mathbf{r}}} \hat{\mathbf{v}}(\hat{\mathbf{r}}) \hat{G}(\hat{\mathbf{r}}, \hat{\mathbf{r}}'; \boldsymbol{\mu}) ds' ds, \quad (51)$$

$$\hat{\mathcal{J}}(\hat{\mathbf{X}}, \hat{\mathbf{v}}; \boldsymbol{\mu}) = \gamma\gamma' \int_{\hat{\Gamma}} \int_{\hat{\Gamma}'} (\mathcal{R}\hat{\mathbf{v}}(\hat{\mathbf{r}})) \cdot \left[ \begin{array}{c} (\mathcal{R}'\hat{\mathbf{X}}(\hat{\mathbf{r}}')) \\ \times \mathbf{grad}_{\hat{\mathbf{r}}} \hat{G}(\hat{\mathbf{r}}, \hat{\mathbf{r}}'; \boldsymbol{\mu}) \end{array} \right] ds' ds, \quad (52)$$

where  $\hat{\mathbf{v}}(\hat{\mathbf{r}}) = (\hat{\mathcal{P}}\mathbf{v})(\hat{\mathbf{r}})$ ,  $\hat{\mathbf{X}}(\hat{\mathbf{r}}') = (\hat{\mathcal{P}}'\mathbf{X})(\hat{\mathbf{r}}')$ , and  $\hat{G}(\hat{\mathbf{r}}, \hat{\mathbf{r}}'; \boldsymbol{\mu})$  have the same form as that described in Eq. (40). The incident terms and far electric field mapped onto the reference boundary can be written as

$$\hat{f}_{E^{\text{inc}}}(\hat{\mathbf{v}}; \boldsymbol{\mu}) = \gamma \int_{\hat{\Gamma}} (\mathcal{R}\hat{\mathbf{v}}(\hat{\mathbf{r}})) \cdot \mathbf{E}^{\text{inc}}(\mathcal{T}(\hat{\mathbf{r}})) ds, \quad (53)$$

$$\hat{f}_{\overline{H}^{\text{inc}}}(\hat{\mathbf{v}}; \boldsymbol{\mu}) = \gamma \int_{\hat{\Gamma}} (\mathcal{R}\hat{\mathbf{v}}(\hat{\mathbf{r}})) \cdot \overline{\mathbf{H}}^{\text{inc}}(\mathcal{T}(\hat{\mathbf{r}})) ds, \quad (54)$$

$$\hat{E}^{\infty}(\hat{\mathbf{J}}, \mathbf{d}_{\text{rcs}}) = \frac{j k_0 \eta_0 \gamma'}{4\pi} e^{jk_0 \mathbf{d}_{\text{rcs}} \cdot \mathbf{t}'} \mathbf{d}_{\text{rcs}} \times \left( \mathcal{R}' \int_{\hat{\Gamma}} \hat{\mathbf{J}}(\hat{\mathbf{r}}') e^{jk_0 \mathbf{d}_{\text{rcs}} \cdot \gamma' \mathcal{R}' \mathbf{r}'} ds' \times \mathbf{d}_{\text{rcs}} \right). \quad (55)$$

Constructing the affine decomposition expression for the function

$$e^{jk_0 \mathbf{d}_{\text{inc}} \cdot \gamma \mathcal{R} \hat{\mathbf{r}}} = \sum_{m=1}^{M_f} \alpha_m^f(\gamma, k_0, \mathcal{R}, \mathbf{d}_{\text{inc}}) \phi_m^f(\hat{\mathbf{r}}), \quad (56)$$

then we have

$$\hat{f}_{E^{\text{inc}}}(\hat{\mathbf{v}}; \boldsymbol{\mu}) = A \sum_{m=1}^{M_f} \Theta_m(\boldsymbol{\mu}) (\mathcal{R}^T \mathbf{p}_E^{\text{inc}}) \cdot \int_{\hat{\Gamma}} \phi_m^f(\hat{\mathbf{r}}) \hat{\mathbf{v}}(\hat{\mathbf{r}}) ds, \quad (57)$$

where  $\Theta_m(\boldsymbol{\mu}) = \gamma e^{jk_0 \mathbf{d}_{\text{inc}} \cdot \mathbf{t}} \alpha_m^f(\gamma, k_0, \mathcal{R}, \mathbf{d}_{\text{inc}})$ . Replacing  $\mathbf{p}_E^{\text{inc}}$  in Eq. (57) by  $\mathbf{p}_{\overline{H}}^{\text{inc}}$ , we can immediately obtain the affine decomposition expression of  $\hat{f}_{\overline{H}^{\text{inc}}}(\hat{\mathbf{v}}; \boldsymbol{\mu})$ . By the same token, constructing an affine decomposition expression for  $e^{jk_0 \mathbf{d}_{\text{rcs}} \cdot \gamma \mathcal{R} \hat{\mathbf{r}}}$  and substituting it into Eq. (55), the calculation of the far electric field can also be decomposed into a parameter-independent offline phase and a parameter-dependent online phase.

Next, we devote ourselves to separate variable parameters from the boundary integral operators described in Eqs. (50)–(52). Since the scatterer considered in Section 2.B consists of only one boundary, which indicates that the transformation operators  $\mathcal{T} = \mathcal{T}'$ , Eqs. (50) and (52) can thereby be written in simple forms as

$$\hat{\chi}^1(\hat{\mathbf{X}}, \hat{\mathbf{v}}) = \gamma^2 \int_{\hat{\Gamma}} \int_{\hat{\Gamma}'} \hat{\mathbf{v}}(\hat{\mathbf{r}}) \cdot \hat{\mathbf{X}}(\hat{\mathbf{r}}') \hat{G}(\hat{\mathbf{r}}, \hat{\mathbf{r}}'; \boldsymbol{\mu}) ds' ds, \quad (58)$$

$$\hat{\mathcal{J}}(\hat{\mathbf{X}}, \hat{\mathbf{v}}) = \gamma^2 \int_{\hat{\Gamma}} \int_{\hat{\Gamma}'} \hat{\mathbf{v}}(\hat{\mathbf{r}}) \cdot \left[ \begin{array}{c} \hat{\mathbf{X}}(\hat{\mathbf{r}}') \\ \times \mathbf{grad}_{\hat{\mathbf{r}}} \hat{G}(\hat{\mathbf{r}}, \hat{\mathbf{r}}'; \boldsymbol{\mu}) \end{array} \right] ds' ds. \quad (59)$$

Decomposing the Green's function and its gradient into the sum of a non-singular part (denoted by "ns") and a singular part leads to

$$\hat{G}(\hat{\mathbf{r}}, \hat{\mathbf{r}}'; \boldsymbol{\mu}) = \gamma^{-1} \hat{G}^{\text{ns}}(\hat{\mathbf{r}}, \hat{\mathbf{r}}'; \boldsymbol{\mu}) + \gamma^{-1} \frac{1}{4\pi |\hat{\mathbf{r}}_0|}, \quad (60)$$

$$\mathbf{grad}_{\hat{\mathbf{r}}} \hat{G}(\hat{\mathbf{r}}, \hat{\mathbf{r}}'; \boldsymbol{\mu}) = \frac{\hat{\mathbf{r}}_0}{4\pi |\hat{\mathbf{r}}_0|} \left( \hat{G}_{\nabla}^{\text{ns}}(\hat{\mathbf{r}}, \hat{\mathbf{r}}'; \boldsymbol{\mu}) + \frac{k^2}{2} + \frac{\gamma^{-2}}{|\hat{\mathbf{r}}_0|^2} \right). \quad (61)$$

Note that  $\hat{G}^{\text{ns}}(\hat{\mathbf{r}}, \hat{\mathbf{r}}'; \boldsymbol{\mu})$  and  $\hat{G}_{\nabla}^{\text{ns}}(\hat{\mathbf{r}}, \hat{\mathbf{r}}'; \boldsymbol{\mu})$  have no singularities when  $\hat{\mathbf{r}} \rightarrow \hat{\mathbf{r}}'$ , and the corresponding affine decomposition expressions constructed by EIM are

$$\mathcal{I}(\hat{G}^{\text{ns}})(\hat{\mathbf{r}}, \hat{\mathbf{r}}'; \boldsymbol{\mu}) = \sum_{m=1}^{M_G^{\text{ns}}} \alpha_{G,m}^{\text{ns}}(\boldsymbol{\mu}) \phi_{G,m}^{\text{ns}}(\hat{\mathbf{r}}, \hat{\mathbf{r}}'), \quad (62)$$

$$\mathcal{I}(\hat{G}_{\nabla}^{\text{ns}})(\hat{\mathbf{r}}, \hat{\mathbf{r}}'; \boldsymbol{\mu}) = \sum_{m=1}^{M_{\nabla}^{\text{ns}}} \alpha_{\nabla,m}^{\text{ns}}(\boldsymbol{\mu}) \phi_{\nabla,m}^{\text{ns}}(\hat{\mathbf{r}}, \hat{\mathbf{r}}'). \quad (63)$$

Substituting Eqs. (62) and (63) into Eqs. (60) and (61), we can get the affine decomposition expressions of the Green's function and its gradient

$$\mathcal{I}(\hat{G})(\hat{\mathbf{r}}, \hat{\mathbf{r}}'; \boldsymbol{\mu}) = \sum_{m=0}^{M_G^{\text{ns}}} \gamma^{-1} \alpha_{G,m}^{\text{ns}}(\boldsymbol{\mu}) \phi_{G,m}^{\text{ns}}(\hat{\mathbf{r}}, \hat{\mathbf{r}}'), \quad (64)$$

$$\mathcal{I}(\text{grad}_{\hat{r}} \hat{G})(\hat{r}; \hat{r}'; \boldsymbol{\mu}) = \sum_{m=-1}^{M_{\hat{v}}^{\text{ns}}} \alpha_{\hat{v},m}^{\text{ns}}(\boldsymbol{\mu}) \frac{\phi_{\hat{v},m}^{\text{ns}}(\hat{r}, \hat{r}') \hat{r}_0}{4\pi |\hat{r}_0|}, \quad (65)$$

where  $\alpha_{G,0}^{\text{ns}}(\boldsymbol{\mu}) = \gamma^{-1}$ ,  $\phi_{G,0}^{\text{ns}}(\hat{r}, \hat{r}') = 1/(4\pi |\hat{r} - \hat{r}'|)$ ;  $\alpha_{\hat{v},-1}^{\text{ns}}(\boldsymbol{\mu}) = k^2$ ,  $\phi_{\hat{v},-1}^{\text{ns}}(\hat{r}, \hat{r}') = 1/2$ ,  $\alpha_{\hat{v},0}^{\text{ns}} = 1$ , and  $\phi_{\hat{v},0}^{\text{ns}}(\hat{r}, \hat{r}') = 1/|\hat{r}_0|^2$ .

Substituting Eqs. (64) and (65) into Eqs. (51), (58) and (59), the integration of all the parameter-independent functions can be calculated in the offline phase. The parameter-independent integral in Eq. (57) could also be calculated in the offline phase. The obtained parameter-independent matrices are then projected into the reduced-basis space. Based on these reduced matrices, we can quickly assemble the reduced-basis model for  $\forall \boldsymbol{\mu} \in \mathcal{D}$ . Substituting the reduced-basis solution into Eq. (55) and considering the corresponding affine decomposition expression, the calculation of far field is also independent of the dimension of the original model.

It is noted that the scatterer considered in Section 2.B only consists of one boundary, which yields  $\mathcal{T} = \mathcal{T}'$ . Here, we will briefly discuss the situation of  $\mathcal{T} \neq \mathcal{T}'$ . In this case, the affine decompositions of  $\hat{\lambda}^1(\hat{\mathbf{X}}, \hat{\mathbf{v}}; \boldsymbol{\mu})$  and  $\hat{\lambda}^2(\hat{\mathbf{X}}, \hat{\mathbf{v}}; \boldsymbol{\mu})$  have been discussed in [30]. Similar to the normal derivative of the 2D Green's function, it is difficult to separate the parameters in  $\hat{\mathcal{Y}}(\hat{\mathbf{X}}, \hat{\mathbf{v}}; \boldsymbol{\mu})$ . Therefore,  $\hat{\mathcal{Y}}(\hat{\mathbf{X}}, \hat{\mathbf{v}}; \boldsymbol{\mu})$  has to be calculated in the online phase, similar to what we have done to the normal derivative of the 2D Green's function in Section 4.A. This operation will also slightly reduce the online efficiency of RB-BEM.

## 5. NUMERICAL EXPERIMENTS

In this section, we first compare the efficiency of improved greedy algorithms with the standard one by constructing affine decomposition expressions for two functions, and then present three numerical examples to examine the RB-BEM for the scattering problems of dielectric scatterers. The in-house computer program used for the simulation is based on MATLAB [version (R2014a)], and run on a workstation equipped with double 2.0 GHz Intel Xeon CPUs. To further demonstrate the capability of our proposed RB-BEM, we also compare the accuracy and computation time of our method with the results achieved by a commercial electromagnetic software, COMSOL Multiphysics [version (5.2)].

### A. Example 1

We construct affine decomposition expressions for two functions, as shown in Eqs. (66) and (67), using Methods 1–4 described in Section 3:

$$f_1(\mathbf{x}; \boldsymbol{\mu}) = \exp\left(-\frac{(x_1 - \mu_1)}{0.02} - \frac{(x_2 - \mu_2)}{0.02}\right) + 1, \quad (66)$$

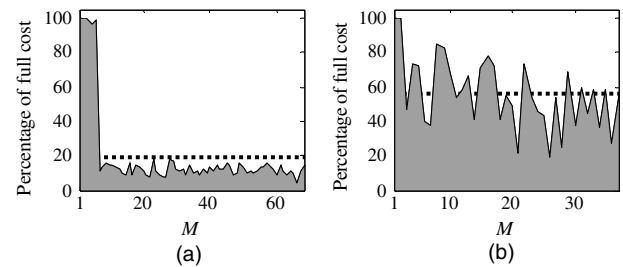
$$f_2(\mathbf{x}; \boldsymbol{\mu}) = \sin(2\pi\mu_1(x_1 - \mu_2)) \sin(2\pi\mu_3(x_2 - \mu_4)) + 2. \quad (67)$$

The spatial variable  $\mathbf{x} = (x_1, x_2) = [0, 1] \times [0, 1]$  for  $f_1$  and  $f_2$ , and the interval  $[0, 1]$  is equidistantly divided into 100 points. For  $f_1$ , the parameter  $\boldsymbol{\mu} = (\mu_1, \mu_2) \in \mathcal{D} = [0, 1] \times [0, 1]$ , and the interval  $[0, 1]$  is equidistantly divided into 10, 15, and 20 points to form three training set  $\Xi_1$ ,  $\Xi_2$ , and  $\Xi_3$ , respectively. For  $f_2$ ,  $\boldsymbol{\mu} = (\mu_1, \mu_2, \mu_3, \mu_4) \in \mathcal{D} = [0, 0.5] \times [1, 1.5] \times [0, 0.5] \times [1, 1.5]$ , we still choose three training

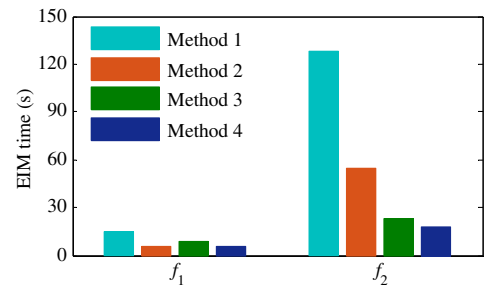
sets, which correspond to 4, 7, and 10 equidistantly distributed points in each interval, respectively. The tolerance  $tol = 1 \times 10^{-5}$ , and the Methods 1 and 2 are both running on the finest training set  $\Xi_3$ .

Figure 1 presents the saving of workload at each step in Method 2. As can be observed, for  $f_1$  and  $f_2$ , the average savings of workload are about 80% and 40%, respectively. Figure 2 presents the comparison of the efficiencies between the standard greedy algorithm (Method 1) and the three improved algorithms (Methods 2–4) in the calculation of the EIM results for  $f_1$  and  $f_2$ . For  $f_1$ , the dimension of the affine decomposition expressions obtained by Methods 1–4 are 67, 68, 69, and 71, respectively, and the corresponding execution times are 14.903, 5.454, 8.927, and 5.685 s. For  $f_2$ , the dimension of the affine decomposition expressions are 36, 37, 37, and 38, respectively, and the corresponding execution times are 127.791, 54.698, 23.134, and 18.137 s.

After testing the affine decomposition expressions on a randomly sampled parameter set  $\Xi_{\text{test}}$  with the same size as  $\Xi_3$ , the results in Table 1 indicate that the accuracy of the three improved greedy algorithms is on the same order of magnitude as that of the standard algorithm. Note that here the accuracy indicator is the maximum of 2-norm of the relative errors between the function  $f$  and its approximation from the affine decomposition expression for  $\forall \boldsymbol{\mu} \in \Xi_{\text{test}}$ . Compared to the standard greedy algorithm, the improved algorithms dramatically decrease the offline workload and online efficiency without loss of accuracy. As can be observed from Fig. 2 and Table 1, Method 4 exhibits a better performance than



**Fig. 1.** Percentage of workload at each step, using the saturation-assumption-based greedy algorithm compared to that of the standard greedy algorithm, for (a)  $f_1$  and (b)  $f_2$ .



**Fig. 2.** Comparison of execution times of the standard greedy algorithm (Method 1) and three improved greedy algorithms (Methods 2–4).

**Table 1. Approximation Accuracy of Four Greedy Algorithms on a Randomly Sampled Parameter Set of Example 1**

Function	Method 1	Method 2	Method 3	Method 4
$f_1$	$2.239 \times 10^{-5}$	$1.679 \times 10^{-5}$	$9.613 \times 10^{-6}$	$1.678 \times 10^{-5}$
$f_2$	$7.640 \times 10^{-6}$	$7.363 \times 10^{-6}$	$5.301 \times 10^{-6}$	$2.401 \times 10^{-6}$

Methods 2 and 3, and is thus used in the following examples to construct the reduced-basis space and affine decomposition expressions.

**B. Example 2**

The scatterer in Example 2 is a 2D Si cylinder with a square cross section, as shown in Fig. 3, immersed in free space. The boundary is divided into quadratic segments. The wavelength of the TE polarized illuminating wave is  $0.4 \mu\text{m}$ , and the corresponding refractive index of Si is  $5.6317 - 0.2858j$ . The amplitude of the incident electric field is 1. The ratio between the radius of the round corners  $R$  and the side length  $L$  is fixed at 0.025. The parameter considered in this example contains the side length  $L$  of the scatterer and the incident angle  $\theta_{\text{inc}}$ , i.e.,  $\mu = (L, \theta_{\text{inc}}) \in \mathcal{D} = [0.2, 0.4] \mu\text{m} \times [0, 90]^\circ$ . Four training sets  $\Xi_1, \Xi_2, \Xi_3,$  and  $\Xi_4$  which consist of rectangular grids with  $26 \times 12, 51 \times 23, 101 \times 45,$  and  $201 \times 91$  points are considered. The tolerance  $tol$  for constructing the affine decomposition expressions and the reduced-basis space are  $1 \times 10^{-5}$  and  $1 \times 10^{-4}$ , respectively.

In this case, the transformation operator at an observation point is identical to that at a source point, i.e.,  $\mathcal{T} = \mathcal{T}'$ , since the scatterer only consists of one boundary. The EIM results of the incident field and the non-singular part of the Hankel functions are presented in Table 2. The subscript “ $b$ ” in  $\hat{H}_{0,b}^{(2),ns}$  and  $\hat{H}_{1,b}^{(2),ns}$  is the region index. The approximation accuracy is

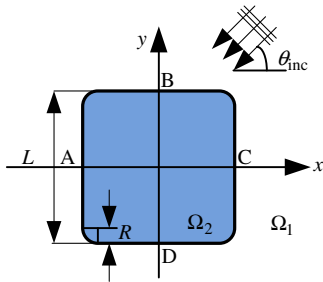


**Fig. 3.** Cross-section of a 2D scatterer in Example 2.

**Table 2. EIM Results for the Parameter-Dependent Functions of Example 2**

Function	$M$	Approximation Accuracy	Execution Time(s)
$u^{\text{inc}}$	29	$6.062 \times 10^{-6}$	1.293
$\hat{H}_{0,1}^{(2),ns}$	8	$3.029 \times 10^{-6}$	19.370
$\hat{H}_{1,1}^{(2),ns}$	8	$1.023 \times 10^{-8}$	23.146
$\hat{H}_{0,2}^{(2),ns}$	13	$1.001 \times 10^{-7}$	28.673
$\hat{H}_{1,2}^{(2),ns}$	15	$1.556 \times 10^{-8}$	32.850

calculated on a randomly sampled parameter set  $\Xi_{\text{test}}$  with the same size as  $\Xi_4$ .

In Table 3, we compared the results of BEM and RB-BEM, including the dimensions of the original model ( $N$ ), the reduced-basis model ( $N$ ), and the time cost in the online phase. For BEM, the time cost in the online phase includes the time to partition the boundary of the scatterer, calculate the impedance matrix and excitation vector, and solve the high-dimensional model. For RB-BEM, the time cost in the online phase includes the time to calculate the coefficients of the affine decomposition expressions, assemble the reduced impedance matrices and reduced excitation vectors obtained in the offline phase, and solve the low-dimensional reduced-basis model. The results indicate that the dimension of the reduced-basis model is only about 10% that of the BEM model, and the computational efficiency of RB-BEM is 35.382 times higher than that of the BEM. Testing the reduced-basis model for  $\forall \mu \in \Xi_{\text{test}}$ , the maximum of 2-norm of the relative errors between the original model solutions and reduced-basis model solution is  $5.714 \times 10^{-4}$ . Figure 4 shows the scattered fields on the boundary calculated by BEM, RB-BEM, and COMSOL for a random parameter  $\mu = (L, \theta_{\text{inc}}) = (0.2904 \mu\text{m}, 35.5081^\circ)$ . As can be observed, the result of RB-BEM is in good agreement with those of BEM and COMSOL. The dimension of the COMSOL model is 220530, and the time taken to solve this model is about 9 s. The 2-norm of the relative errors between the reduced-basis model solution and that of COMSOL is  $2.139 \times 10^{-3}$ . Compared to COMSOL, the computational

**Table 3. Dimension of the Models and the Time Cost in the Online Phase of BEM and RB-BEM of Example 2**

Method	Dimension of Model	Time Cost in the Online Phase(s)		
		Calculate EIM Coefficients	Assemble Model	Solve Model Total
BEM	944	/	1.888	0.058 1.946
RB-BEM	100	0.007	0.047	0.001 0.055

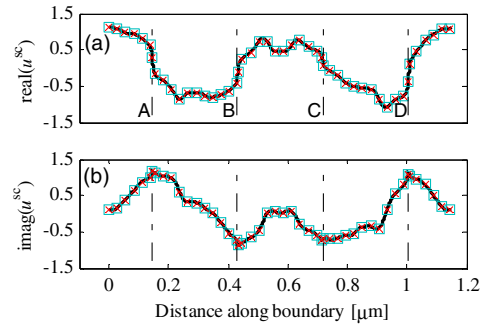


**Fig. 4.** Distribution of scattered fields on the boundary calculated by BEM, RB-BEM, and COMSOL Multiphysics for  $(L, \theta_{\text{inc}}) = (0.2904 \mu\text{m}, 35.5081^\circ)$ : (a) real part; (b) imaginary part. The green square markers and red cross markers represent the BEM and RB-BEM results on the boundary, respectively. The black solid line represents the COMSOL result. The symbols A, B, C, and D denote the intersection points of the boundary and the coordinate axes, as shown in Fig. 3.

efficiency of our RB-BEM is improved by more than 163 times.

### C. Example 3

The scatterer in Example 3 is a 2D cylinder scatterer, immersed in free space, as shown in Fig. 5. The boundaries are divided into segments by quadratic elements. The radius of the Si cylinder is  $0.3 \mu\text{m}$ . The parameter considered in this example contains the thickness of the  $\text{SiO}_2$  layer and  $\text{Si}_3\text{N}_4$  layer, the wavelength and the incident angle of the TE polarized illuminating wave, i.e.,  $\boldsymbol{\mu} = (t_1, t_2, \lambda, \theta_{\text{inc}}) \in \mathcal{D} = [0.1, 0.15] \mu\text{m} \times [0.1, 0.15] \mu\text{m} \times [0.5, 0.55] \mu\text{m} \times [0, 90]^\circ$ . The amplitude of the incident electric field is 1. Three training sets  $\Xi_1$ ,  $\Xi_2$ , and  $\Xi_3$ , which consist of rectangular grids of  $3 \times 3 \times 6 \times 6$ ,  $6 \times 6 \times 11 \times 11$ , and  $26 \times 26 \times 26 \times 46$  points, are considered. The tolerance  $\text{tol}$  for constructing the affine decomposition expressions and the reduced-basis space are  $1 \times 10^{-5}$  and  $1 \times 10^{-4}$ , respectively.

In this case, the transformation operators on three boundaries are different. If the observation point and the source point are located on the same boundary, then  $\mathcal{T} = \mathcal{T}'$ , we need to construct affine decomposition expressions for the non-singular part of the Hankel functions. Otherwise, we need to directly construct the affine decomposition expressions for the Hankel functions. Note that the boundaries are well separated and that the argument of the Hankel function is always larger than  $\tau = 0.02$ , as we recommend in Section 4. Therefore, the Hankel functions are always smooth in the case of  $\mathcal{T} \neq \mathcal{T}'$ .

The dimensions of the affine decomposition expressions of (non-singular part) Hankel functions range from 8 to 12. The dimensions of the affine decomposition expressions of  $u_1^{\text{inc}}$ ,  $u_2^{\text{inc}}$ , and  $u_3^{\text{inc}}$  are 20, 24, and 27, respectively. In Table 4, we compared the result of BEM to that of the RB-BEM. The results indicate that the dimension of the reduced-basis model is only

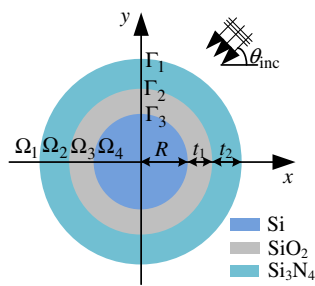


Fig. 5. Cross section of the 2D scatterer in Example 3.

Table 4. Dimension of the Models and the Time Cost in the Online Phase of BEM and RB-BEM of Example 4

Method	Dimension of Model	Time Cost in the Online Phase(s)			Total
		Calculate EIM Coefficients	Assemble Model	Solve Model	
BEM	2176	/	7.134	0.469	7.603
RB-BEM	265	0.028	1.488	0.005	1.521

about 12.2% that of the original model, and the computational efficiency of RB-BEM is about five times higher than that of the BEM.

It is noted that, although the value  $N/\mathcal{N}$  in this example is close to that in Example 2, the online computational efficiency of RB-BEM in this example is only about 1/7 of that in Example 2. According to the analysis in Section 4, this is mainly because the reduced-basis model in Example 2 is independent of  $\mathcal{N}$ , while in this example some integrations about the normal derivative of the Green's function have to be calculated in the online phase. In this example, the numbers of discrete points on three boundaries are very close to each other, and the workload of integration on them are nearly the same. In the BEM process, we need to do 12 integral operations about  $\mathcal{S}$  and  $\mathcal{F}$ , as defined in Eqs. (2) and (3), where two integral operations about  $\mathcal{F}$  cannot be decomposed into the sum of parameter-independent forms and parameter-dependent scalar functions. Therefore, about 1/6 of the workload in the original model cannot be further decreased, which is in accordance with the simulation result.

We then test the reduced-basis model for  $\forall \boldsymbol{\mu} \in \Xi_{\text{test}}$ , where  $\Xi_{\text{test}}$  is a randomly sampled parameter set with the same size as  $\Xi_3$ . The maximum of 2-norm of the relative errors between the solutions of the original and reduced-basis models is  $4.983 \times 10^{-4}$ . Figure 6 shows the scattered fields on the boundaries, along the clockwise direction from the intersections of the boundaries and the negative  $x$ -axis, for a random parameter  $\boldsymbol{\mu} = (t_1, t_2, \lambda, \theta_{\text{inc}}) = (0.1137 \mu\text{m}, 0.1435 \mu\text{m}, 0.5392 \mu\text{m}, 81.0328^\circ)$ . As can be observed, the result of RB-BEM is also in good agreement with that of BEM. The dimension of the COMSOL model is 264707, and the time taken to solve this model is about 14 s. The 2-norm of the relative errors between the reduced-basis model solution and that of COMSOL is  $4.264 \times 10^{-3}$ . Compared to COMSOL, the computational efficiency of our RB-BEM is improved by more than nine times, even though the efficiency of RB-BRM is also slightly reduced in this example.

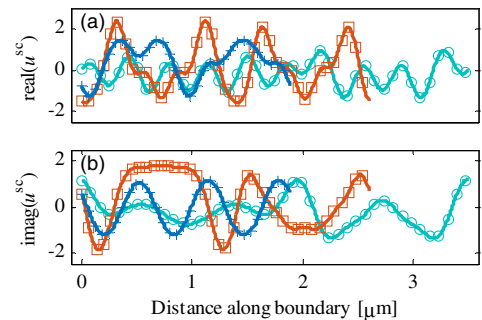


Fig. 6. Distribution of scattered fields on boundaries, along the clockwise direction from the intersections of boundaries and the negative  $x$  axis, calculated by BEM and RB-BEM for  $((t_1, t_2, \lambda, \theta_{\text{inc}}) = (0.1137 \mu\text{m}, 0.1435 \mu\text{m}, 0.5392 \mu\text{m}, 81.0328^\circ)$ : (a) real part; (b) imaginary part. The green, red, and blue lines represent the BEM results for  $\Gamma_1$ ,  $\Gamma_2$ , and  $\Gamma_3$ , respectively, and the circle, square, and cross markers respectively represent the RB-BEM results for boundaries  $\Gamma_1$ ,  $\Gamma_2$ , and  $\Gamma_3$ .

**D. Example 4**

The scatterer in Example 4 is a 3D dielectric cube with a side length of 0.01 m, as shown in Fig. 7, immersed in free space. The cube is rotated around the  $z$  axis with an angle  $\theta \in [0, 90]^\circ$ . The incident plane wave, with the electric field  $\mathbf{E}^{\text{inc}}$  polarized along the  $x$  axis, propagates in the  $y$ - $z$  plane, i.e.,  $\theta_{\text{inc}} \in [0, 90]^\circ$ ,  $\varphi_{\text{inc}} = 90^\circ$ . The free-space wavelength of the incident field is fixed at 0.02 m. The relative permittivity of the scatterer is 2. The boundary is divided into small patches by RWG elements. The interested output is the monostatic RCS signal, which means the receiving angles of the RCS signal are identical to the incident angles. Therefore, the parameters considered are the rotation angle of the scatterer and the incident angle of the plane wave. Three training sets  $\Xi_1$ ,  $\Xi_2$ , and  $\Xi_3$ , which consist of rectangular grids of  $21 \times 21$ ,  $41 \times 41$ , and  $81 \times 81$  points, are considered. The tolerance  $tol$  for constructing the affine decomposition expressions and the reduced-basis space are  $1 \times 10^{-3}$  and  $1 \times 10^{-2}$ , respectively.

In this case, the transformation operator at an observation point is identical to that at a source point, i.e.,  $\mathcal{T} = \mathcal{T}'$ , since the scatterer only consists of one boundary. The dimension of the affine decomposition expression in Eq. (56) is 138. The dimensions of the affine decomposition expressions in Eqs. (62) and (63) are 54 and 78 in the interior region of the scatterer, and 77 and 95 in the exterior region. The dimensions of the original model and the reduced-basis model are 8504 and 391, respectively. In this example, the online efficiency of RB-BEM is determined by the dimensions of the affine decomposition expressions and the dimension of reduced basis space. For any new parameter, the online computation time of RB-BEM is 5.144 s.

The approximation accuracy is calculated on a randomly sampled parameter set  $\Xi_{\text{test}}$  with the same size as  $\Xi_3$ .

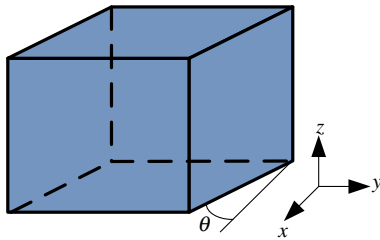


**Fig. 7.** 3D cubic scatterer used in Example 4.

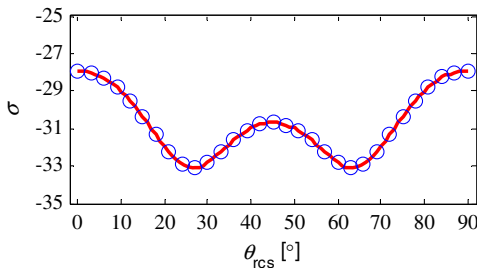


**Fig. 8.** Monostatic RCS signal for  $\theta = 0.0029^\circ$ . The red solid line and blue circle represent the BEM and RB-BEM results, respectively.

Testing the reduced-basis model for  $\forall \mu \in \Xi_{\text{test}}$ , the maximum of 2-norm of the relative errors between the solutions of the original and reduced-basis models is  $3.435 \times 10^{-2}$ . Figure 8 shows the monostatic RCS signal for a random rotation angle  $\theta = 0.0029^\circ$ . One finds that the result of RB-BEM is also in agreement with that of BEM. The dimension of the COMSOL model is 1164120, and the time taken to solve this model is about 170 s. The 2-norm of the relative errors between the reduced-basis model solution and that of COMSOL is  $7.329 \times 10^{-2}$ . Compared to COMSOL, the computational efficiency of our RB-BEM is improved by nearly 30 times.

**6. CONCLUSIONS**

In this work, the RB-BEM is proposed to realize efficient modeling of parameterized electromagnetic scattering problems for dielectric scatterers. The presented method splits the high-dimensional original model into parameter-dependent and parameter-independent parts based on the affine assumption of parameter-dependent functions, and further projects the off-line part of the original model into a low-dimensional reduced-basis space in the offline phase. Then, in the online phase, one only needs to calculate the coefficients of the interpolation expressions and assemble the low-dimensional reduced-basis model based on the reduced offline parts to solve it. In the implementation of RB-BEM, the greedy algorithm is commonly used to construct the affine decomposition expressions of parameter-dependent functions and the low-dimensional reduced-basis space. The principle of the greedy algorithm is training an approximate space over a parameter training set until the approximate accuracy approaches the prescribed tolerance, which typically results in considerable computational effort, especially in a large size training set. We propose an improved greedy algorithm based on multiple training sets with increasing sizes, and further considering the saturation assumption. The numerical experiments indicate that the efficiency of the improved greedy algorithm is several times higher than the standard one.

It is noted that the affine decomposition expressions for parameter-dependent functions should be constructed carefully, especially for the Green's function and its normal derivative or gradient function. If the transformation operator of the observation point  $\mathbf{r}$  is identical to that of the source point  $\mathbf{r}'$ , i.e.,  $\mathcal{T} = \mathcal{T}'$ , all the parameter-dependent functions can be decomposed into the sum of parameter-dependent scalar functions multiplied by parameter-independent forms. Therefore, the reduced-basis model is independent of the dimension of the original model, and the online efficiency is exclusively determined by the dimensions of affine decomposition expressions and the dimension of reduced-basis space. Note that the online efficiency is slightly reduced in the case of  $\mathcal{T} \neq \mathcal{T}'$ , since a part of integral operations have to be calculated in the online phase. However, even so, the online efficiency of RB-BEM is still demonstrated to be several times higher than that of the BEM.

In this paper, for the sake of simplicity, we take isotropic scatterers as examples to elaborate the RB-BEM. It is noted that, for scatterers with different material or feature characteristics, if the scatters can be modeled correctly by BEM, and the

manifolds of BEM solution and parameter-dependent functions are smooth enough, our proposed RB-BEM is expected to be available. Further work will focus on extending the method to more general cases.

**Funding.** National Natural Science Foundation of China (NSFC) (51405172, 51475191, 51525502, 51575214).

**Acknowledgment.** The author is thankful for the efforts and useful discussions with Dr. Jinlong Zhu, who is now a postdoctoral researcher at University of Illinois at Urbana-Champaign (UIUC).

## REFERENCES

1. A. Oskooi, A. Mutapcic, S. Noda, J. D. Joannopoulos, S. P. Boyd, and S. G. Johnson, "Robust optimization of adiabatic tapers for coupling to slow-light photonic-crystal waveguides," *Opt. Express* **20**, 21558–21575 (2012).
2. S. Zhou, W. Li, G. Sun, and Q. Li, "A level-set procedure for the design of electromagnetic metamaterials," *Opt. Express* **18**, 6693–6702 (2010).
3. X. Chen, S. Liu, C. Zhang, H. Jiang, Z. Ma, T. Sun, and Z. Xu, "Accurate characterization of nanoimprinted resist patterns using Mueller matrix ellipsometry," *Opt. Express* **22**, 15165–15177 (2014).
4. V. F. Paz, S. Peterhansel, K. Frenner, and W. Osten, "Solving the inverse grating problem by white light interference Fourier scatterometry," *Light Sci. Appl.* **1**, e36 (2012).
5. L. Li, "New formulation of the Fourier modal method for crossed surface-relief gratings," *J. Opt. Soc. Am. A* **14**, 2758–2767 (1997).
6. M. G. Moharam, E. B. Grann, D. A. Pommet, and T. K. Gaylord, "Formulation for stable and efficient implementation of the rigorous coupled-wave analysis of binary gratings," *J. Opt. Soc. Am. A* **12**, 1068–1076 (1995).
7. P. Monk, *Finite Element Methods for Maxwell's Equations* (Oxford University, 2003).
8. A. Taflov and S. C. Hagness, *Computational Electrodynamics: The Finite-Difference Time-Domain Method* (Artech House, 2004).
9. D. Colton and R. Kress, *Integral Equation Methods in Scattering Theory* (SIAM, 2013).
10. K. Hirayama, E. N. Glytsis, and T. K. Gaylord, "Rigorous electromagnetic analysis of diffractive cylindrical lenses," *J. Opt. Soc. Am. A* **13**, 2219–2231 (1996).
11. J. M. Bendickson, E. N. Glytsis, T. K. Gaylord, and A. F. Peterson, "Modeling considerations for rigorous boundary element method analysis of diffractive optical element," *J. Opt. Soc. Am. A* **18**, 1495–1506 (2001).
12. A. J. Poggio and E. K. Miller, "Integral equation solutions of three-dimensional scattering problems," in *Computer Techniques for Electromagnetics*, R. Mittra, ed. (Permagon, 1973), pp. 159–264.
13. T. K. Wu and L. L. Tsai, "Scattering from arbitrarily-shaped lossy dielectric bodies of revolution," *Radio Sci.* **12**, 709–718 (1977).
14. S. M. Rao, D. R. Wilton, and A. W. Glisson, "Electromagnetic scattering by surfaces of arbitrary shape," *IEEE Trans. Antennas Propag.* **30**, 409–418 (1982).
15. Y. Chang and R. F. Harrington, "A surface formulation for characteristic modes of material bodies," *IEEE Trans. Antennas Propag.* **25**, 789–795 (1977).
16. F. Arndt, J. Brandt, V. Catina, J. Ritter, I. Rullhusen, J. Dauelsberg, U. Hilgert, and W. Wessel, "Fast CAD and optimization of waveguide components and aperture antennas by hybrid MM/FE/MoM/FD methods—state-of-the-art and recent advances," *IEEE Trans. Microw. Theory Tech.* **52**, 292–305 (2004).
17. C. J. Reddy, M. D. Deshpande, C. R. Cockrell, and F. B. Beck, "Fast RCS computation over a frequency band using method of moments in conjunction with asymptotic waveform evaluation technique," *IEEE Trans. Antennas Propag.* **46**, 1229–1233 (1998).
18. P. Bradley, C. Brennan, and M. Condon, "Efficient wideband electromagnetic scattering computations for frequency dependent lossy dielectrics using WCAWE," *IEEE Trans. Antennas Propag.* **57**, 3274–3282 (2009).
19. C. Y. Wu and H. M. Hou, "An efficient transient modeling for 3-D multi-level interconnections in a stratified dielectric medium," *Solid-State Electron.* **42**, 1881–1891 (1998).
20. Z. Q. Zhang, Q. H. Liu, C. Xiao, E. Ward, G. Ybarra, and W. T. Joines, "Microwave breast imaging: 3-D forward scattering simulation," *IEEE Trans. Biomed. Eng.* **50**, 1180–1189 (2003).
21. A. K. Noor and J. M. Peters, "Reduced basis technique for nonlinear analysis of structures," *AIAA J.* **18**, 455–462 (1980).
22. J. P. Fink and W. C. Rheinboldt, "On the error behavior of the reduced basis technique for nonlinear finite element approximation," *ZAMM Z. Angew. Math. Mech.* **63**, 21–28 (1983).
23. C. Prud'homme, D. V. Rovas, K. Veroy, L. Machiels, Y. Maday, A. T. Patera, and G. Turinici, "Reliable real-time solution of parametrized partial differential equations: reduced-basis output bound methods," *J. Fluids Eng.* **124**, 70–80 (2002).
24. K. Veroy, *Reduced-basis methods applied to problems in elasticity: analysis and applications*, Ph.D. thesis (Massachusetts Institute of Technology, 2003).
25. G. Rozza, D. B. P. Huynh, and A. T. Patera, "Reduced basis approximation and a posteriori error estimation for affinely parametrized elliptic coercive partial differential equations," *Arch. Comput. Methods Eng.* **15**, 229–275 (2008).
26. A. Quarteroni, G. Rozza, and A. Manzoni, "Certified reduced basis approximation for parametrized partial differential equations and applications," *J. Math. Ind.* **1**, 1–49 (2011).
27. J. S. Hesthaven, G. Rozza, and B. Stamm, *Certified Reduced Basis Methods for Parametrized Partial Differential Equations* (Springer, 2016).
28. J. Pomplun and F. Schmidt, "Accelerated a posteriori error estimation for the reduced basis method with application to 3D electromagnetic scattering problems," *SIAM J. Sci. Comput.* **32**, 498–520 (2010).
29. M. W. Hess and P. Benner, "Fast evaluation of time-harmonic Maxwell's equations using the reduced basis method," *IEEE Trans. Microw. Theory Tech.* **61**, 2265–2274 (2013).
30. Y. Chen, J. S. Hesthaven, Y. Maday, J. Rodriguez, and X. Zhu, "Certified reduced basis method for electromagnetic scattering and radar cross section estimation," *Comput. Methods Appl. Mech. Eng.* **233–236**, 92–108 (2012).
31. M. Fares, J. S. Hesthaven, Y. Maday, and B. Stamm, "The reduced basis method for the electric field integral equation," *J. Comput. Phys.* **230**, 5532–5555 (2011).
32. M. Ganesh, J. S. Hesthaven, and B. Stamm, "A reduced basis method for electromagnetic scattering by multiple particles in three dimensions," *J. Comput. Phys.* **231**, 7756–7779 (2012).
33. M. Barrault, Y. Maday, N. C. Nguyen, and A. T. Patera, "An 'empirical interpolation' method: application to efficient reduced-basis discretization of partial differential equations," *C. R. Acad. Sci. Paris I* **339**, 667–672 (2004).
34. M. A. Grepl, Y. Maday, N. C. Nguyen, and A. T. Patera, "Efficient reduced-basis treatment of nonaffine and nonlinear partial differential equations," *ESAIM Math. Model. Numer. Anal.* **41**, 575–605 (2007).
35. D. J. Knezevic and J. W. Peterson, "A high-performance parallel implementation of the certified reduced basis method," *Comput. Methods Appl. Mech. Eng.* **200**, 1455–1466 (2011).
36. B. Haasdonk, M. Dihlmann, and M. Ohlberger, "A training set and multiple bases generation approach for parametrized model reduction based on adaptive grids in parameter space," *Math. Comput. Model. Dyn. Syst.* **17**, 423–442 (2011).
37. J. S. Hesthaven, B. Stamm, and S. Zhang, "Efficient greedy algorithm for high-dimensional parameter spaces with application to empirical interpolation and reduced basis methods," *ESAIM Math. Model. Numer. Anal.* **48**, 259–283 (2014).
38. M. Abramowitz and I. A. Stegun, *Handbook of Mathematical Functions with Formulas, Graphs, and Mathematical Tables* (Dover, 1964).